Sustainable Structures
ISSN: 2789-3111 (Print); ISSN: 2789-312X (Online)
http://www.sustain-dpl.com/journal/sust
DOI: 10.54113/j.sust.2026.000115

ORIGINAL ARTICLE

Experimental investigation on failure behavior of a novel high-tensile FRP-metal crimped thread connection

Longfa Wang[a], Dongdong Zhang[a,*], Ruijie Zhu[a], Yifeng Gao[a,*], Chenxi Lv[a], Weite Shi[b]
[a]College of Field Engineering, Army Engineering University of PLA, Nanjing 210007, P. R. China
[b]Fuzhou Regional Military Representative Office of PLA, Fuzhou 350000, P. R. China
[*]Corresponding Author. Dongdong Zhang. Email: zhangdodo_163@163.com
Yifeng Gao. Email: sky_blue68@163.com

Abstract: A novel fiber-reinforced polymer (FRP)-metal crimped thread connection (FMCTC) is developed for lightweight emergency truss bridge system constructed with pultruded FRP tubes. Experimental investigations were conducted to evaluate the feasibility, manufacturability, tensile behavior, and failure mechanisms of this new composite connection. The results reveal that the design successfully eliminates secondary processing and specialized tooling of parent FRP tubes; instead, composite threads are efficiently formed via passive crimping equipment. By integrating spiral-crimped thread geometry with preloaded high radial pressure, the specimens achieve 65% connection efficiency relative to base FRP strength. Two dominant failure modes are identified: (i) primary shear failure of the crimped FRP threads followed by interfacial slippage, and (ii) secondary failure patterns involving localized cross-sectional fractures coupled with longitudinal cracking in extended FRP tubes. Notably, despite distinct failure modes, all specimens exhibit minimal variation in ultimate loads. The substantial bearing strength, reaching up to 836.3 MPa, is governed by the shear resistance mechanism of the FRP threads. Owing to its manufacturing simplicity, enhanced connection efficiency, and exceptional load-bearing capacity, the newly developed FMCTC offers a viable technical solution for practical deployment in lightweight emergency truss bridge systems.

Keywords: fiber-reinforced polymer (FRP), composite connection, truss bridge, thread, crimping technology, failure tensile test, failure mechanism

1 Introduction

Pultruded fiber-reinforced polymer (FRP) tubular elements exhibit pronounced unidirectional characteristics [1,2], achieving optimal load transfer along the fiber orientation axis—making them well-suited for axial load-bearing applications in space truss assemblies. A critical design consideration for hybrid FRP-metal truss systems is establishing reliable connections between the FRP elements and metallic counterparts [3-15]. Conventional joining methods—adhesive [16-20], mechanical bolted [21-25], and riveted connections [26-29]—suffer from intrinsic deficiencies in connection efficiency and load-bearing capacity, leading to structural overdesign and material redundancy. These drawbacks particularly hinder their application in mass-critical, heavy-load, deployable FRP truss bridges where stringent weight optimization is essential. Consequently, developing structurally efficient, high-bearing capacity FRP-to-metal connections remains a pivotal technical challenge for advancing high-performance truss bridges.

Received: 2 December 2025; Received in revised form: 15 June 2026; Accepted: 8 July 2026

A composite pre-tightened tooth connection (PTTC) was developed to enhance joint performance, with successful applications in heavily loaded truss structures [30-33]. This composite connection employs an FRP tube with sparse circumferential grooves and stripe-shaped teeth that mechanically interlock with matching metal teeth on the interior surface of the metal tube. The enhanced load-bearing capacity stems from the FRP's high interlaminar shear stress and the radial compressive stress that enhances interlaminar shear strength. However, the fabrication necessitates secondary processing of base FRP tubes and custom production of grooved FRP teeth, leading to complex manufacturing and high costs. Moreover, pre-formed grooves can cause longitudinal fiber fractures, compromising cross-section integrity and initiating defects at tooth interfaces. The constrained geometry of FRP teeth fundamentally limits the application of substantial radial pressure, thereby hindering the attainment of higher load-bearing capacities [34-38].

To eliminate secondary processing of thin-walled FRP tube and simplify manufacturing, a crimped composite spline joint (CCSJ) was specifically developed [39]. However, the CCSJ exhibited relatively low connection efficiency, with experimental values ranging from 51.2% to 61.3%. In this study, a new composite connection—termed the FRP-Metal crimped thread connection (FMCTC)—is introduced to achieve higher connection efficiency and load-bearing capacity than the CCSJ, while retaining a simple manufacturing process. The conceptual design of the proposed FMCTC is described, followed by quasi-static tensile tests to examine its mechanical behavior and underlying failure mechanism.

2 Description of the FRP-Metal Connection

Fig. 1 illustrates the three-dimensional configuration of the proposed FMCTC for a heavy-load, lightweight truss bridge built with FRP pultruded circular tubes. The FRP-metal connection comprises three concentric layers: an interlayered FRP tube, an outer metal threaded sleeve, and an inner metal lining sleeve. The outer sleeve features circumferential internal threads (triangle or trapezoidal) with specific pitch, thread height, thread angle, and thread diameter. The FRP tube has no pre-formed threads on its outer surface, and the inner sleeve is entirely non-threaded.

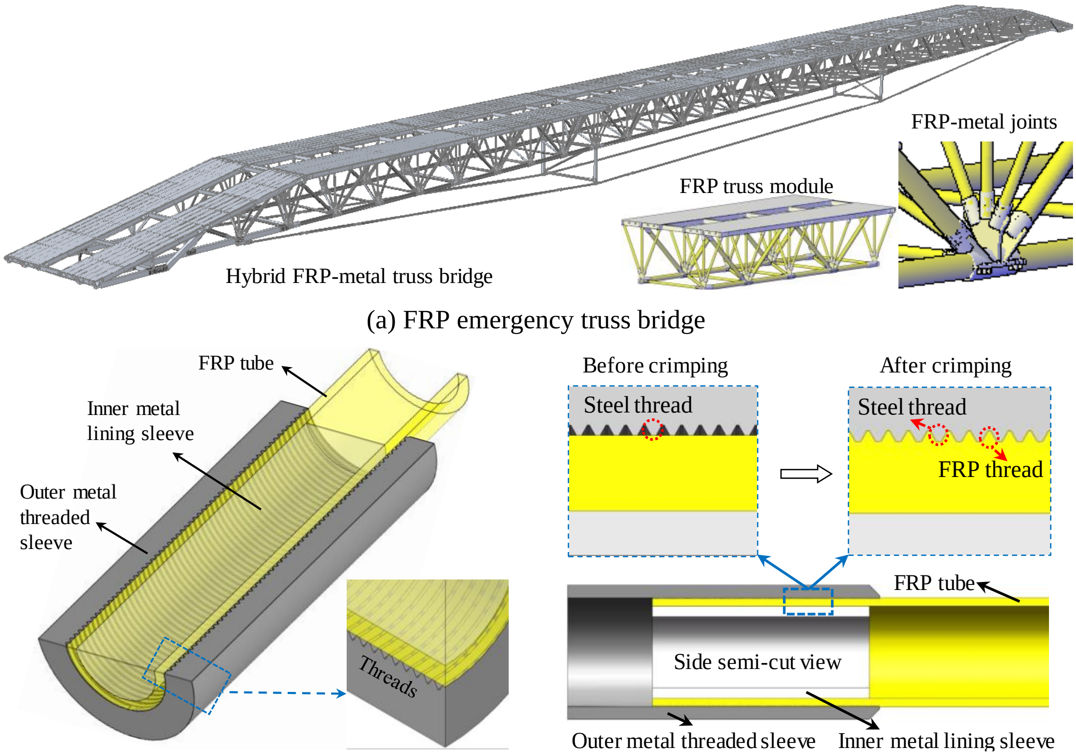

(b) FRP-metal crimped thread connection

Fig. 1. Conceptual designs of the FRP-metal crimped thread connection for the truss bridge.

Structural integration between FRP and metallic components is achieved via a cold-forming crimping process. Prior to crimping, dimensional compatibility is ensured between the root diameter of the outer sleeve's internal threading and the nominal outer diameter of the FRP tube. The inner liner is oversized relative to the FRP tube's inner dimension, creating a designed interference fit. During crimping, a substantial external radial compression is applied on the outer sleeve, inducing both elastic and plastic deformation within its outer surface while driving inward radial contraction of its internal wall. This controlled deformation causes the metal threads to progressively penetrate into the FRP tube, forming geometrically interlocked composite threads, as depicted in **Fig. 1b**.

Notably, composite threads exist only at the interface between the outer sleeve and the FRP tube. Under axial loading, the external force is applied to the outer sleeve at one end of the truss bar, then transferred via shear through the threaded interface to the FRP tube, and finally transmitted to the outer sleeve at the other end in the reverse manner. Since there is no direct connection structure between the inner sleeve and the outer sleeve, the inner sleeve carries no axial load and undergoes neither slip nor shear transfer. Its primary role in the joint design is to provide radial support, thereby mitigating the risk of FRP tube wall fracture induced by circumferential crimping stresses. Hence, only a moderate level of radial stiffness is required for the inner sleeve. To reduce the overall weight of the joint, aluminum alloy was finally selected for the inner sleeve.

Compared to existing PTTC designs with sparse serrated or rectangular grooves [30–38], the proposed FMCTC features densely arranged triangle or trapezoidal threads. The smaller thread pitch allows more small-sized threads per unit length, significantly increasing the metal–FRP interfacial shear area. Moreover, the passive formation of low-height threads eliminates compressive damage to the FRP teeth—a critical advantage given FRP's low transverse strength—while also allowing higher radial force to be applied to the outer sleeve and FRP tube. Additionally, the reduced thread height minimizes weakening of the FRP tube's cross-section, thereby preserving its longitudinal fibers. Collectively, these improvements enhance the performance of the FRP-metal connection.

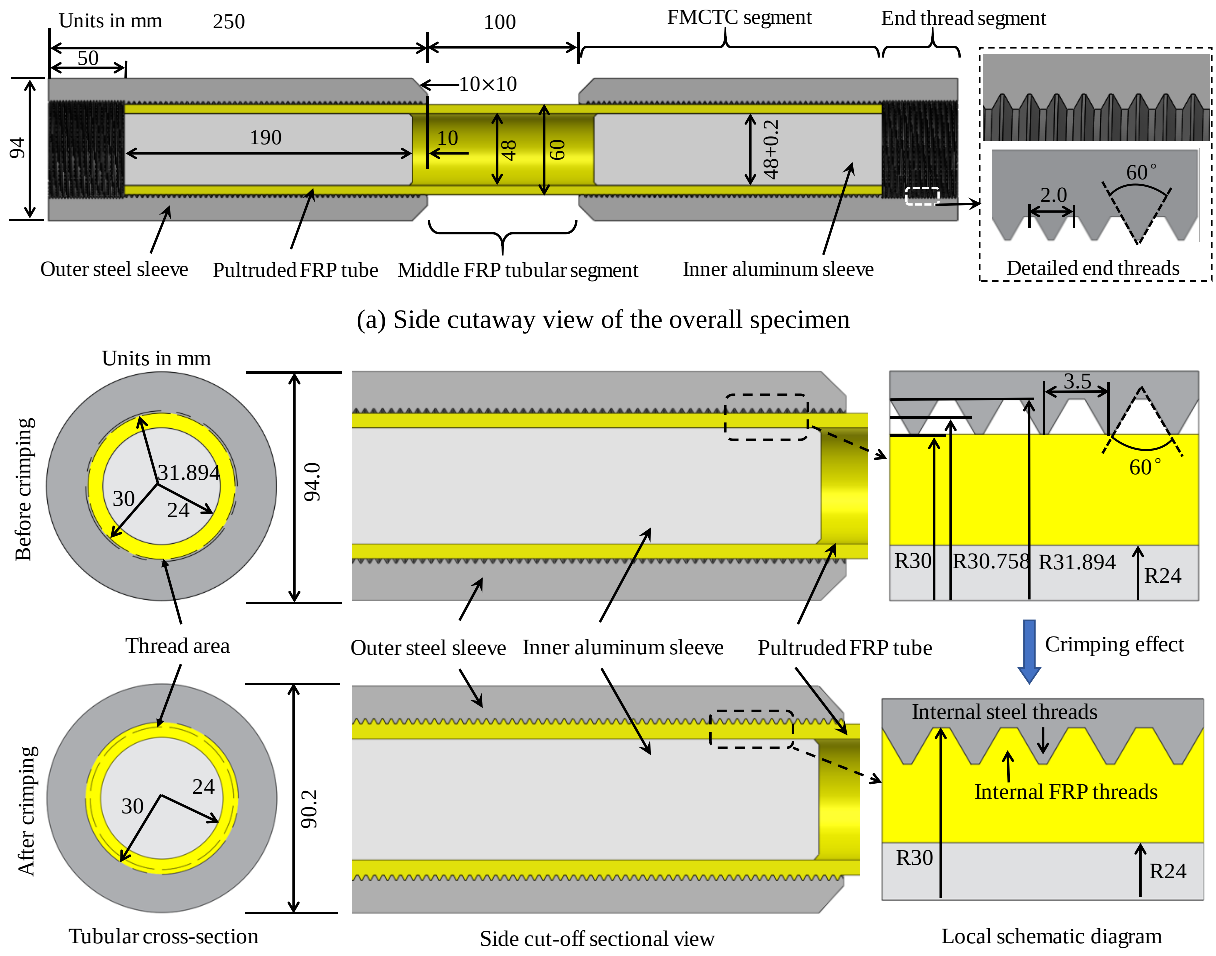

(a) Side cutaway view of the overall specimen

(b) Detailed cutaway view of the local structure of crimped threads

Fig. 2. Geometric dimensions of the designed FRP-metal crimped thread connection.

3 Specimen Preparation

3.1 Specimen Design

To evaluate the tensile performance advantages of the proposed FMCTC, four specimens were designed and labeled as S*i* (where *i*=1, 2, 3, 4), as shown in **Fig. 2**. Each specimen consists of an FRP circular tube and two FMCTCs. Prior to assembly, the FRP tube measured 500 mm in length, 60 mm in diameter, and 6 mm in thickness. The hollow outer sleeves are 200 mm long, with an outer diameter of 94 mm and an inner diameter of 60 mm. The hollow inner sleeves are 190 mm long, with an outer diameter of 48.2 mm and an inner diameter of 16 mm. A 0.1 mm interference fit was thus provided at the interface between the inner sleeve and the FRP tube. To facilitate connection to the testing machine, each of the outer sleeve was extended outward by 50 mm, and threads were implemented on its inner wall. Consequently, the total length of the specimen is 600 mm. This length is primarily limited by space constraints of the testing machine for long tubular specimens.

Within the connection segment, the inner wall of the 200-mm outer sleeve features evenly spaced trapezoidal threads (60° thread angle) with a pitch of 3.464 mm, an external diameter of 63.789 mm, an intermediate diameter of 61.516 mm, and an internal diameter of 60.000 mm. The radial crimping variable is 1.7 mm. In the 50-mm extended jointing segment, the outer sleeves also have incorporated trapezoidal threads with the same 60° angle, but with different dimensions: pitch of 2.000 mm, external diameter of 65.000 mm, intermediate diameter of 63.701 mm, and internal diameter of 62.835 mm. This difference arises because the extended segment is not subjected to crimping pressure; thus, larger thread dimensions are required to transmit axial force.

At the opposite end of the connection near the middle FRP segment, the outer sleeve extends approximately 10.0 mm beyond the inner sleeve. Both sleeves are chamfered at this end: the inner sleeve features a chamfer of approximately 5.0 mm (length) × 2.0 mm (width), and the outer sleeve a chamfer of 10.0 mm × 10.0 mm. These design features are intended to prevent transverse shearing fracture of the longitudinal fibers near this end during the crimping process.

In the specimens, the outer sleeves were made of Q345 steel tube, while the inner sleeves were made of 6061-T6 aluminum alloy. The pultruded FRP tubes were manufactured using hybrid fiber reinforced polymer (FRP) supplied by China Nanjing Jinglue FRP Co., Ltd. The hybrid FRP consists of E-glass and T300 carbon fibers embedded in polyurethane. The fibers make up approximately 80% per weight, with about 44% glass fiber and 36% carbon fiber. The mechanical properties of the FRP materials, as provided by the manufacturer, are detailed in **Tab. 1**. In the table, E_{ij} (i= 1, 2, 3) represent the elastic modulus in the three principal directions, G_{ij} (i =1, 2, 3) denote the shear modulus in the three principal planes, and v_{ij} (i= 1, 2, 3) represent the Poisson's ratios.

Table 1. Mechanical properties of the used FRP and metal materials

Materials	Elastic modulus E (GPa)	Poisson's ratio v	Strength (MPa)
FRP	E_1 = 120.0; E_2 = E_3 = 10.2; G_{12} = G_{13} = 5.7; G_{23} = 4.8	v_{12} = v_{13} = 0.26 v_{23} = 0.2	S_{11} = 1287.3; S_{22} = S_{33} = 110.0; S_{12} = S_{13} = 61.9; S_{23} = 30.5
Steel Q345	210	0.3	$f_{0.2}$ = 345; f_u = 470; f_c = 414
Al 6061-T6	68.9	0.33	$f_{0.2}$ = 240; f_u = 265

Note: '1' represents the fiber direction, while '2' and '3' correspond to directions perpendicular to the fiber orientation of the pultruded FRP tube.

3.2 Fabrication Procedure

The manufacturing procedure for the proposed FMCTC comprised three phases:

Phase 1: Component Preparation (**Fig.3a**). The FRP tubes were fabricated using a pultrusion machine. Per the manufacturer's requirements, the diameter tolerance was specified as ±0.5 mm, the wall thickness tolerance as ±0.2 mm, and the roundness deviation (out-of-roundness) as ≤0.5% of the nominal diameter. The FRP tubes were cut to specified lengths using conventional machining.

Note: both the aluminum and steel sleeves were machined from solid bar stock via lathe turning. Due to budget constraints in this study, all components were fabricated by small, low-cost machining workshops. Owing to limited research experience, we did not request the workshop to provide diameter tolerances, thickness tolerances, or roundness deviations during specimen production. Consequently, the workshop did not supply these precise parameters throughout the course of this study. For future large-scale production and practical applications, these manufacturing tolerances and roundness deviations must be given particular attention to ensure product reliability.

(a) Preparation the FRP tube, inner and outer metal sleeves of the specimen

(b) Assembly of the inner sleeve (c) Crimping of the outer sleeve

Fig. 3. Fabrication process of the designed FRP-metal crimped thread connection.

Phase 2: Inner Sleeve Installation (**Fig.3b**). The inner sleeves were axially press-fitted into the FRP tube, achieving a consistent interference fit of 0.1 mm. A hydraulic press system was used to ensure coaxial alignment between the sleeve and the host tube during assembly. Prior to insertion, a thin lubricant layer was applied to the exterior of the sleeves to facilitate smooth interfacial contact.

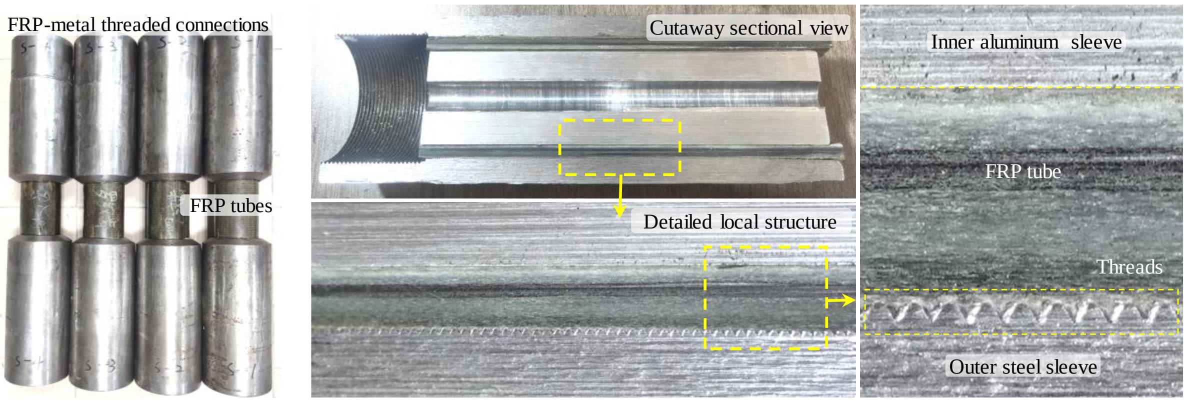

(a) Actual test pieces (b) Cutaway view of the detailed local structure of crimped threads

Fig. 4. Fabricated specimens of the FRP-metal crimped thread connection.

Phase 3: Crimping Assembly (**Fig.3c**). Final assembly used a KM-91F-500 radial crimping apparatus with programmable pressure regulation. The eight-blade crimping system with evenly distributed compression elements enabled circumferential deformation of the outer sleeves. Key parameters included precise alignment of sleeve-tube interfaces and maintained end-plane parallelism. Process controls ensured consistent crimping displacements across all specimens.

Achieving uniform crimping parameters across test specimens was challenging due to instrument precision limits (±0.1 mm) and inherent variations in FRP tube wall thickness. To overcome this, a constant crimping pressure of 25.0 MPa was maintained throughout the process, rather than applying crimping variables. Post-crimping measurements showed a mean radial deformation of 1.65 mm across all specimens.

The fabricated specimens are shown in **Fig. 4a**, with **Fig. 4b** detailing the connection interface. Post-crimping observations indicate effective integration of the FRP tube with the aluminum and steel sleeves. The trapezoidal steel threads left well-defined impressions on the FRP outer wall, creating complementary deformations and forming matching composite threads. However, some plastic distortion was observed at the tips of the steel threads, which may affect interfacial shear behavior and axial load transfer in the FRP-metal connection.

4 Experimental Program

4.1 Experimental Layout

To examine the tensile behavior of the FRP-Metal connection, a quasi-static failure tests was conducted on specimens using a universal testing machine (UTM), as shown in **Fig. 5**. Axial tensile loading was applied via a specially designed fixed steel connecting piece that linked the tubular specimens to the UTM. This connecting piece comprised a gripping section (clamped by the UTM) and a screw thread segment (connected to the 50-mm extended end of the specimen's outer steel sleeve). Loading was displacement-controlled at a rate of 1.0 mm/min. Prior to formal loading, a preload of 200 kN was applied to verify proper operation of the equipments and to eliminate any gaps between components.

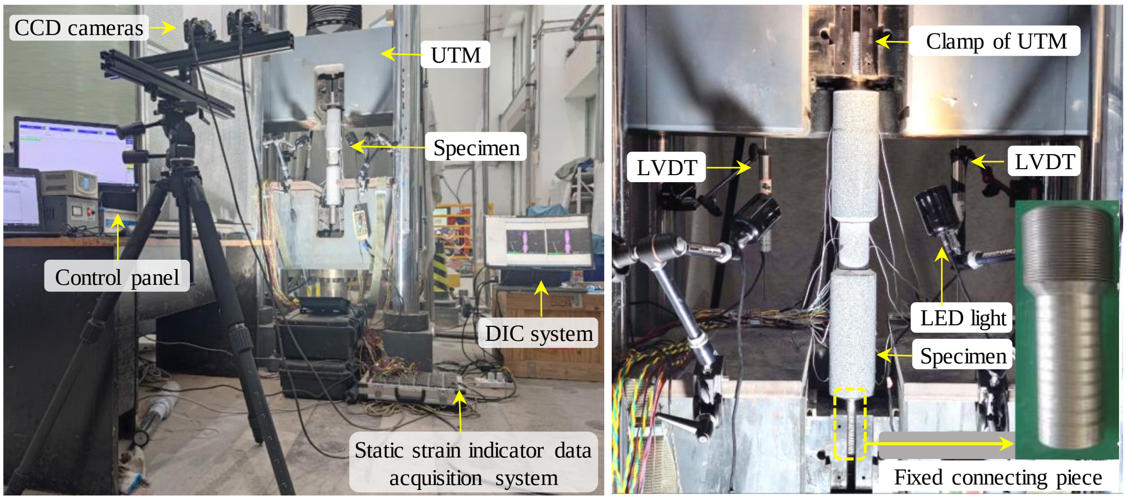

Fig. 5. Experimental setup for quasi-static tensile loading of the FRP-metal connection.

4.2 Instrumentation

As illustrated in **Fig. 6**, the experiment instrumented failure modes, displacement, and strain response. Failure modes were documented using cameras and visual observation. The UTM automatically recorded load-displacement curves and ultimate bearing capacity at a data acquisition rate of 1.0 Hz. Axial displacement was also measured using two linear variable differential transformers (LVDTs; range: 100 mm, accuracy: 0.001 mm), symmetrically placed on the upper loading tablet of the UTM. These two LVDTs also served to monitor whether the upper loading tablet remained level.

A digital image correlation (DIC) system was used to capture full-field surface strains on the tubular specimens. For this purpose, the front semi-circular surface was polished, coated with white matte paint, and then decorated with black speckle patterns using water transfer printing technology. DIC images were taken by charge-coupled device (CCD) cameras at a sampling rate of 1 Hz, and the collected data were analyzed with VIC-3D software.

On the opposite semi-circular surface, unidirectional resistance strain gauges were attached along the axial direction to measure longitudinal strains. These gauges were placed on six cross‑sections: four (C1–C4) on the end outer sleeves and two (C5–C6) on the middle FRP tube. At each cross‑section, three gauges (labeled A–C) were evenly spaced counterclockwise. Data from the strain gauges and LVDTs were synchronously recorded by a static strain indicator data acquisition system.

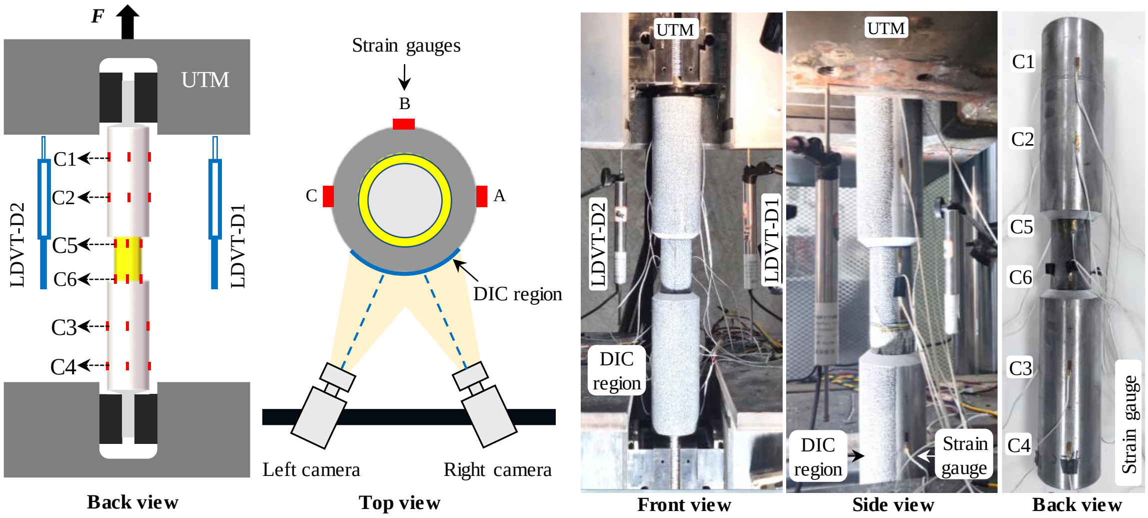

(a) Schematic diagram (b) On-site measurement

Fig. 6. Instrumentation scenario for quasi-static tensile loading of the FRP-metal connection.

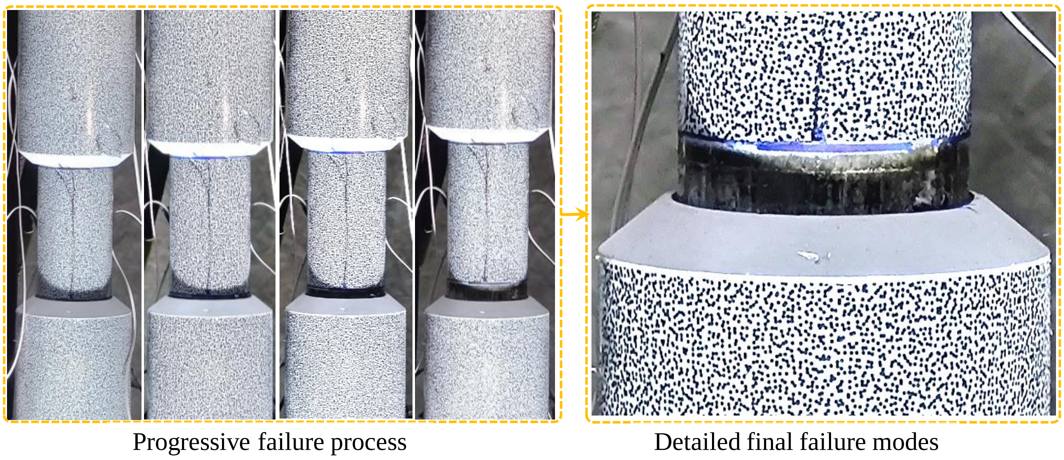

(a) Specimen S1 and S2

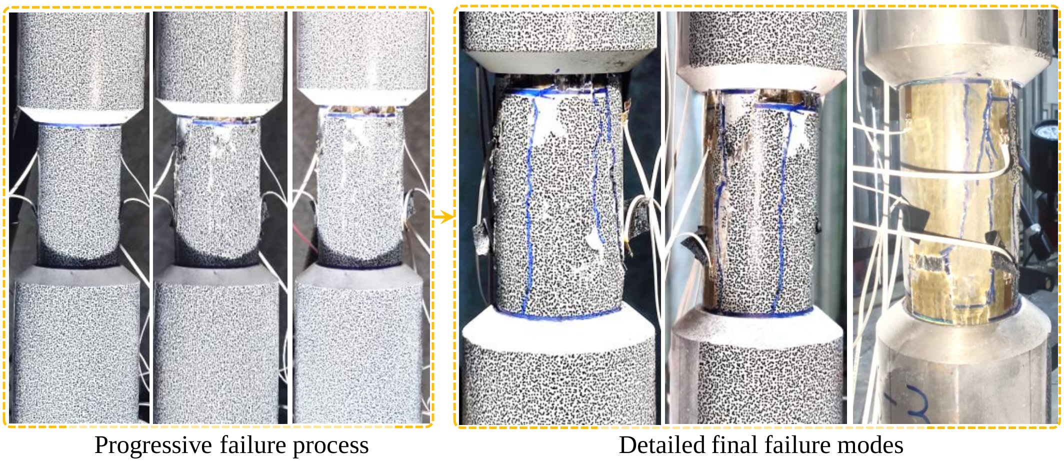

(b) Specimen S3 and S4

Fig. 7. Progressive failure modes of the FRP-metal crimped thread connections.

5 Experimental Results

5.1 Failure Modes

Two representative progressive failure modes of the FMCTCs were observed: specimens S1 and S2 exhibited one mode (**Fig. 7a**), while S3 and S4 displayed the other (**Fig. 7b**). For S1 and S2, the failure mode was characterized by progressive interfacial slippage between the interlayered FRP tube and the outer steel sleeve of the bottom FMCTC. It is noted that the interfacial FRP layers had already sustained damage, with the originally smooth surface showing evident roughness, shallow pits, and local damage. As indicated in **Fig. 4b**, a key cause of this interface failure was shear failure of the FRP threads embedded in the steel threads of the outer sleeve. In other words, shear failure of the FRP threads occurred prior to the progressive interfacial slippage.

In contrast, S3 and S4 exhibited localized sectional fracture and several longitudinal cracks in the FRP tube. Specifically, localized fiber fracture occurred at the junction of the FRP tube inside the outer sleeve (on the front surface with sprayed speckles), while no fiber fractures were observed on the back surface, leaving a relatively neat notch. This resulted from transverse compression during crimping of the outer sleeve, which induced certain transverse shear failure and initial localized damage to the FRP tube at the junction. Simultaneously, crimping might cause cross-sectional irregularities near the junction between the FRP tube and the outer sleeve, deviating longitudinal FRP fibers from straight alignment and generating stress concentration under axial load. The combined effect of initial damage and stress concentration ultimately led to localized fiber rupture and fracture notches.

Following localized fiber rupture and sectional fracture, axial loading was transmitted unevenly along the FRP tube. In this case, the centroid axis deviated from the external loading point, subjecting the tubular cross-section to combined tension and bending—i.e., eccentric loading. Consequently, the non-ruptured tensioned side experienced higher axial stress, while the opposite side bore lower stress. When the higher-stressed side reached its tensile strength, additional fiber fracture occurred, leading to subsequent longitudinal cracking of the FRP tubular cross-section. This substantial longitudinal cracking compromised the integrity of the hybrid FRP tube, resulting in uneven pullout of a partial segment of the interlayered FRP tube.

5.2 Load–Displacement Responses

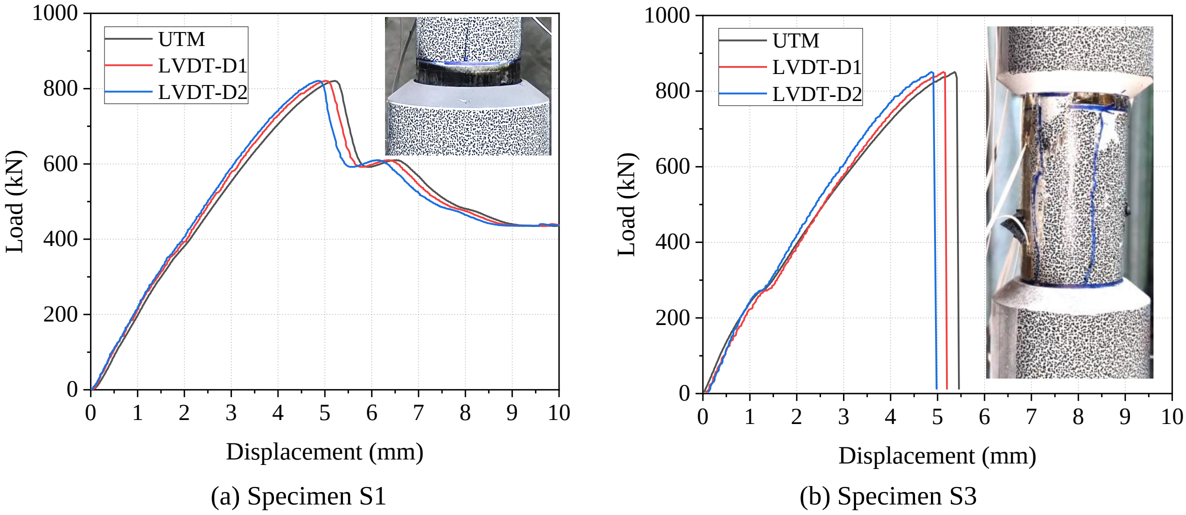

Fig. 8. Load–displacement curves of the experimental FRP-metal crimped thread connections.

Fig. 8 illustrates the load–displacement curves from the UTM and LVDTs. For brevity, only subplots S1 and S3 are presented; S2 and S4 are omitted because their failure modes and curves are similar to those of S1 and S3, respectively. The three sensor curves for each specimen exhibit consistent trends, with UTM displacement slightly larger than LVDT readings at all loading levels. At peak load, the displacement discrepancies (UTM vs. average LVDT) were 0.27 mm (5.19%) for S1 and 0.37 mm

(6.86%) for S3. These minor discrepancies arise from testing errors (e.g., sensor precision variation and local stiffness differences in the UTM) and confirm the accuracy of both measurements.

For specimens S1 (and similarly S2), the two LVDT curves are consistent up to ultimate load, indicating minimal eccentric loading and uniform axial deformation of the tubular cross-section. This aligns with the observed failure modes (shear failure of FRP threads and progressive interfacial slippage) and is confirmed by DIC (Fig. 9a). In contrast, specimens S3 and S4 exhibit a growing discrepancy between the two LVDT readings with increasing load, which become apparent at ultimate load. This reflects significant eccentric loading and non-uniform axial deformation, as confirmed by DIC (Fig. 9b). Such eccentric loading likely contributed to partial section fracture and longitudinal cracks, unlike the interfacial shear damage and progressive slippage seen in S1 and S2.

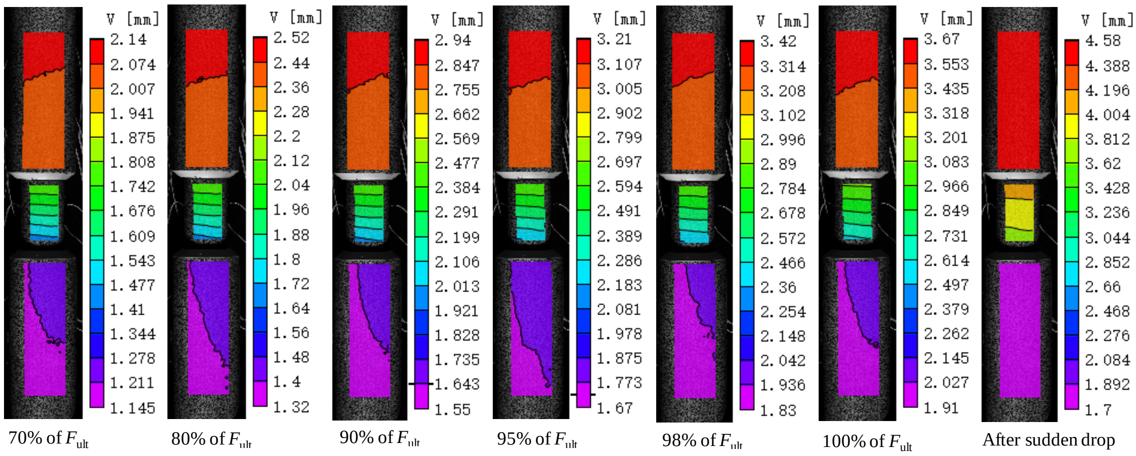

(a) Specimen S1

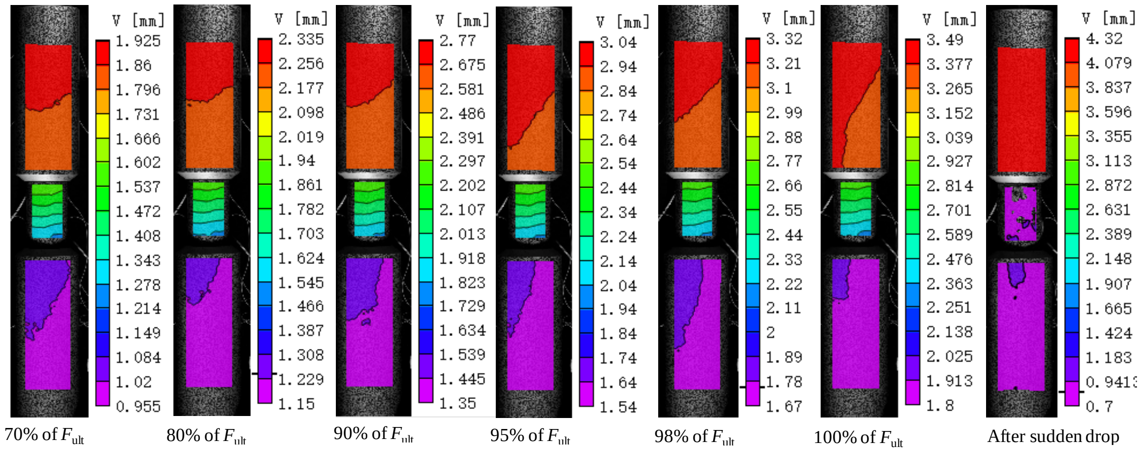

(b) Specimen S3

Fig. 9. Axial deformation measured using the DIC system during the loading process of the specimens.

Fig. 9 shows that for S1, axial deformation along the upper FMCTC exhibits good uniformity throughout loading up to the ultimate load, with a distinct and relatively regular boundary between the upper one-third and lower two-thirds of the upper FMCTC. In contrast, for specimen S3, deformation became significantly non-uniform as loading approached 95% of ultimate load F_{ult}, indicating eccentric loading on the upper FMCTC. For both S1 and S3, the lower FMCTCs exhibit non-uniform axial deformation with opposite directions on the left and right sides, implying opposing eccentric loading on the lower connections prior to ultimate load. However, after a sharp post-peak load drop, neither the upper nor the lower connections exhibit eccentric loading or non-uniform axial deformation within the outer steel sleeves. The middle FRP tubes remain nearly uniformly deformed throughout. Thus, the varied eccentric or axial loading among components led to the distinct failure modes.

Fig. 10 compares the UTM load-displacement curves for all specimens. Two distinct trends are observed. For S3 and S4, loading increases nearly linearly with displacement until the peak load, where an audible cracking noise occurs, followed by an abrupt drop to zero. This abrupt change corresponds to fiber fracture and longitudinal cracks in the middle FRP tubes (**Fig. 7b**). No slippage occurs at the tubular interface during the drop, indicating that the passively crimped FRP threads remain intact without shearing failure at that moment.

For S1 and S2, the pre-peak linear trend is similar to that of S3 and S4, indicating comparable axial stiffness. However, near the peak load, S3 and S4 produce gradual, intermittent destructive sounds, unlike the sudden, audible fracture sounds of S1 and S2. These noises coincide with local curvature shifts near the peak load (moderate for S1/S2 [black/red lines]; abrupt for S3/S4 [blue/pink lines]), as shown in the local block diagram. After the peak, S1 and S2 do not drop abruptly; instead, load decreases gradually and then stabilizes at a constant level, reflecting their failure modes (**Fig. 7a**). Specifically, the sudden decrease indicates shear failure in FRP threads within a specific segment. As shear failure progresses, FRP matrix and fiber debris accumulate at the tubular interface. This accumulation, along with incomplete thread shearing and friction, likely enables the specimens to maintain a certain load and relative stability.

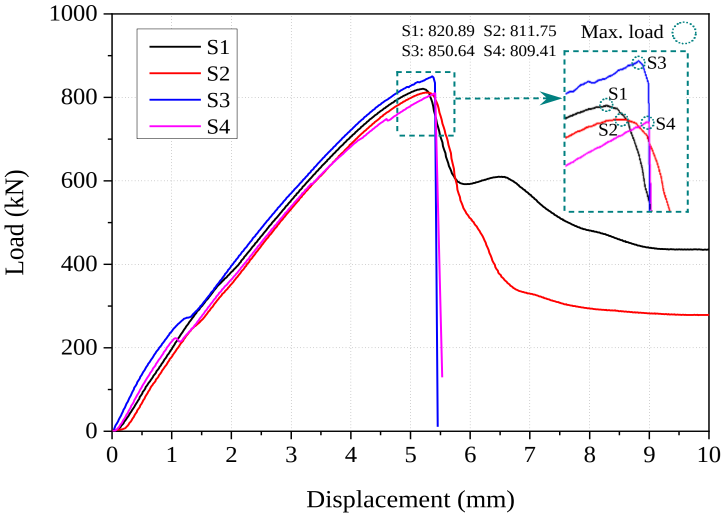

Fig. 10. Comparison of the experimental load–displacement curves of all specimens.

Table 2. Primary tensile strength indicators of the testing FRP-Metal crimped thread connection

Specimen Mumber	Ultimate Loads F_{ult} (kN)	Bearing Strength σ_b, ult (MPa)	Connection Efficiency (%)	Failure Modes
S1	820.9	806.5	62.7	Thread shear failure and interfacial slippage
S2	811.7	797.5	61.9	Thread shear failure and interfacial slippage
S3	851.2	836.3	65.0	Local sectional fracture and longitudinal cracks
S4	809.1	794.9	61.8	Longitudinal cracks and sectional fracture
AVG.	823.2	808.8	62.8	-

5.3 Load–Strain Responses

The ultimate loads (F_{ult}) extracted from the load-displacement curves are summarized in **Tab. 2**. The bearing strength $\sigma_{b,ult}$, defined as the ratio of the ultimate load to the cross-sectional area of the FRP tube, and the connection efficiency, defined as the ratio of the bearing strength to the FRP material strength, are subsequently calculated. Despite different failure modes, the bearing strengths show limited variability across the four specimens. Specifically, S1 and S2 exhibit maximum and minimum capacities of 806.5 MPa and 797.5 MPa, respectively, while S3 and S4 yield 836.3 MPa and 794.9 MPa. The discrepancy between the higher strengths of S1 and S3 is around 3.56%, and that between the lower capacities of S2 and S4 is approximately 0.32%. The developed FMCTC achieves a minimum connection efficiency of 61.8% and a maximum of 65.0%.

5.3.1. Strains within the Outer Steel Sleeves

For conciseness, S1 and S3 are selected for strain analysis due to their higher load-bearing capacities and representative failure modes. **Fig. 11** and **Fig. 12** depict the load-strain curves from strain gauges on the outer steel sleeves, respectively. For clarity, strain data up to the peak load for the four tubular cross-sections (C1–C4) are plotted separately, alongside average strains for comparison.

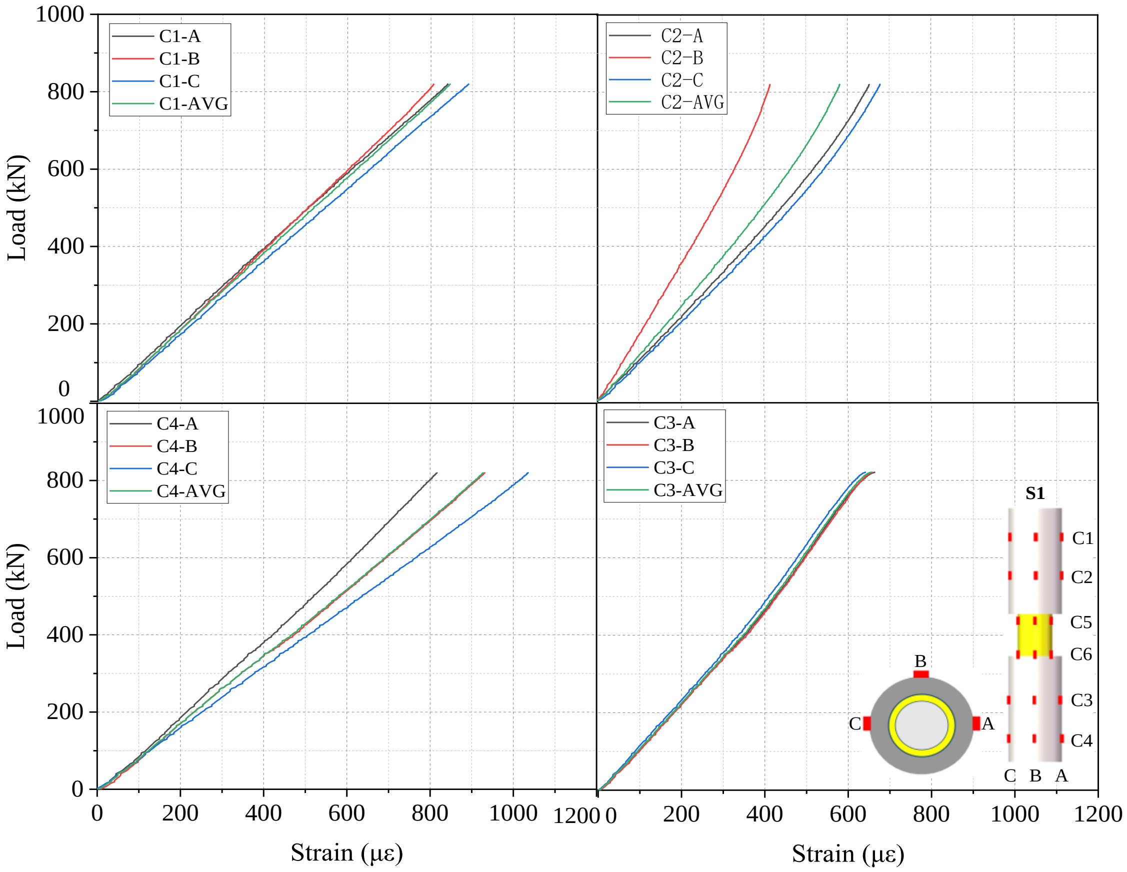

Fig. 11. Load–strain curves measured by strain gauges positioned on the outer steel sleeve of specimen S1.

For S1 (**Fig. 11**), it is found that strain discrepancies among points A, B, and C on most cross-sections gradually increase with load. Notably, positive axial strains on the same cross-section are inconsistent, with varying discrepancies along the four sections. The largest discrepancies occur at C2 and C3 (263.4 με and 218.4 με, respectively), while C1 and C4 show minimal discrepancies (84.4 με and 22.1 με). At peak load, strain ratios (A/B and C/B) are: 1.58 and 1.64 at C2; 0.88 and 1.11 at C4; 1.04 and 1.10 at C1; and 1.01 and 0.98 at C3, indicating non-ideal axial tension. Moreover, in C1, C2, and C4, point C consistently exhibits the highest strain among the three points. Strains at A exceed B in C1 and C2, but B exceeds A in C4. For C1 and C4, the average strain closely matches point B, indicating a stress state similar to pure bending in the A-C plane. Conversely, C2 displays a discrepancy between the average strain and point B, implying a more complex strain state involving bending both within and perpendicular to the A-C plane. Thus, specimen S1 did not undergo ideal axial tensile loading; rather, it exhibited uneven load transfer and a complex strain state—an atypical behavior under standard laboratory tensile conditions.

In specimen S3 (**Fig. 12)**, axial strain discrepancies on identical cross-sections increase with load and are observed across all four cross-sections (C1–C4)—not just C2 and C4—indicating that the strain non-uniformity is more severe than in S1. The maximum discrepancies at C1, C2, C3, and C4 are 309.3 με, 102.4 με, 284.7 με, and 297.1 με, respectively. Except at C2, these values exceed those of S1 (84.4, 263.4, 22.1, and 218.4 με), indicating a more complex, non-ideal axial tensile state. Consistent with S1, sections C1 and C4 show average strains (points A, B, C) closely matching point B, suggesting pure bending in the A-C plane. In contrast, C2 and C3 exhibit a discrepancy between the average strain and point B, implying additional bending perpendicular to the A-C plane. Additionally, strain distribution varies: at C1 and C2, point C records the highest strain and point A the lowest; at C3 and C4, point B is highest and point C lowest. At peak load, strain ratios (A/B and C/B) are 0.81 and 1.19 for C1; 0.86 and 1.00 for C2; 0.98 and 0.64 for C3; and 0.85 and 0.72 for C4. These ratios reveal that the upper connection of S3 undergoes opposite bending in the A‑C plane relative to the lower connection, distinguishing it from S1.

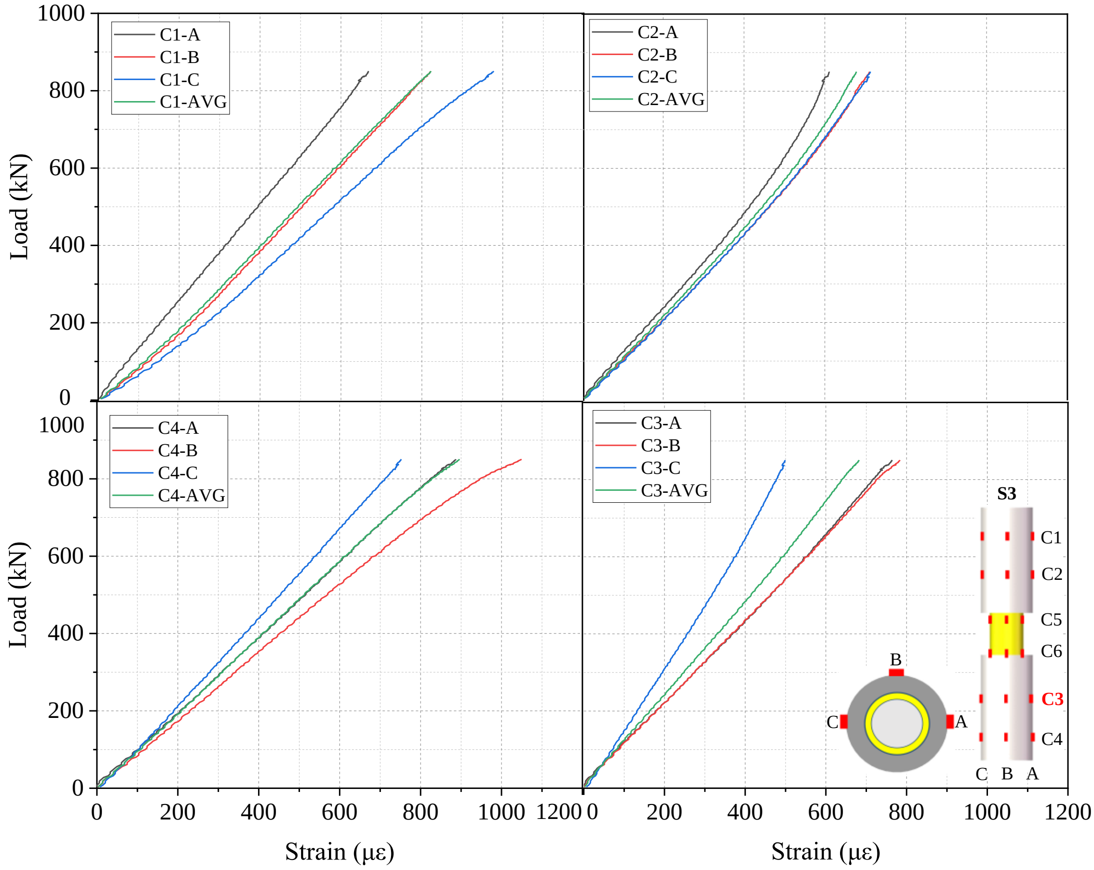

Fig. 12. Load–strain curves measured by strain gauges positioned on the outer steel sleeve of specimen S3.

Fig. 13 presents the average axial strains on each tubular cross-section of specimens S1 and S3. Up to the peak load, both specimens show significantly larger strains at C4 and C1 than at C3 and C2. For S1, strains at C4 and C1 are 927.44 με and 846.24 με, respectively, compared to 655.45 με (C3) and 580.90 με (C2), yielding ratios of 1.41 (C4/C3) and 1.46 (C1/C2). For S3, strains at C4 and C1 are 896.42 με and 822.54 με, respectively, versus 682.26 με (C3) and 677.97 με (C2), with ratios of 1.31 and 1.21, respectively. These findings indicate that the end FMCTCs transmit a greater load closer to the outer segments than to the inner ones. In comparison, S1 exhibited higher average strains at C1 and C4 than S3 (≈1.03 times) but lower strains at C2 and C3 (0.86 and 0.96 times, respectively). If only axial tension were applied, S1 would be expected to sustain a higher ultimate load; however, Section 4.2 reveals that S3 actually endured a greater ultimate load, implying the presence of bending. The pronounced discrepancies between symmetric sections (C1 vs. C4, and C2 vs. C3) confirm that bending significantly influenced the tensile behavior of the end FMCTCs.

The maximum measured strain and stress under ultimate load are summarized in **Tab. 3**. For specimen S1, the peak axial strain (1034.88 με at point C, cross‑section C4) corresponds to a stress of 217.32 MPa—well below the yield strength of Q345 steel (345 MPa)—confirming that the outer steel sleeve did not yield. Consequently, the pre‑peak nonlinearity in the load–strain curve possibly arises from nonlinear contact at the threaded interface (e.g., shear deformation, local compression of FRP threads) or shear damage to a few FRP threads, rather than from steel failure. For specimen S3, the maximum strain (1049.54 με at point B, cross‑section C4) yields a stress of 220.40 MPa, still far below the yield strength, again indicating the absence of yielding. The nonlinearity in this case likely stems from premature partial thread failure and nonlinear contact deformation. Unlike S1, S3 exhibits more severe bending and a complex strain state, leading to localized sectional fracture and longitudinal cracks rather than FRP thread shear failure or interfacial slippage.

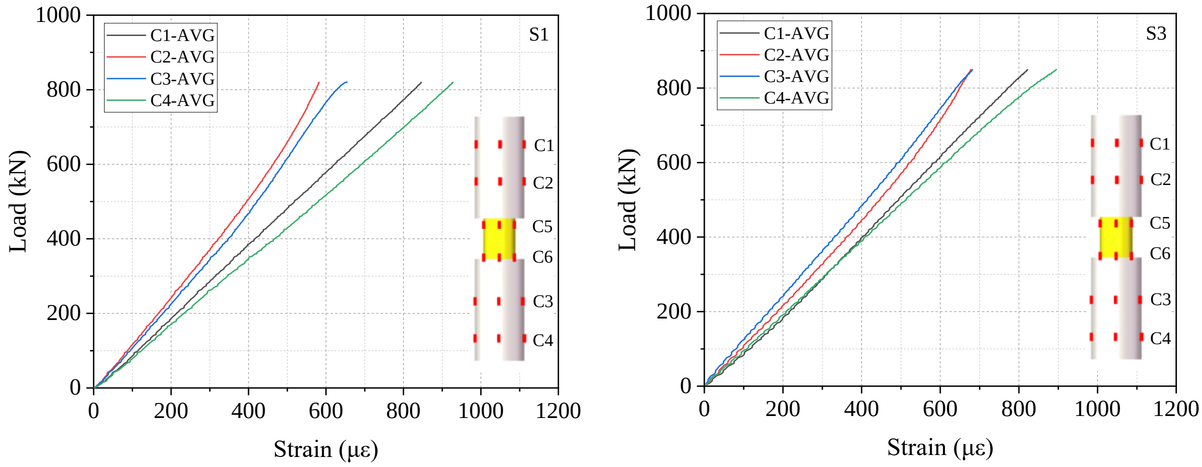

(a) Specimen S1 (b) Specimen S3

Fig. 13. Average strain curves for each tubular cross-section of the outer steel sleeves.

Table 3. Measured maximum strain and stress values on outer steel sleeves under ultimate load

Specimen Number	Section Number	Measured Point Strains (με)				Measured Point Stresses (MPa)			
		A	B	C	Avg.	A	B	C	Avg.
S1	C1	840.94	806.71	891.07	846.24	176.60	169.41	187.12	177.71
	C2	651.77	413.76	677.17	580.90	136.87	86.89	142.21	121.99
	C3	664.89	658.70	642.77	655.45	139.63	138.33	134.98	137.64
	C4	816.53	930.91	1034.88	927.44	171.47	195.49	217.32	194.76
S3	C1	668.28	821.75	977.59	822.54	140.34	172.57	205.29	172.73
	C2	610.49	710.59	712.84	677.97	128.20	149.70	149.70	142.37
	C3	764.33	783.55	498.90	682.26	160.51	164.55	104.77	143.27
	C4	887.27	1049.54	752.45	896.42	186.33	220.40	158.01	188.25

5.3.2. Strains within the Middle FRP Tubes

Fig. 14 presents the load–strain curves for the FRP segments of S1 and S3 up to the ultimate load. For clarity, strain data for the two tubular cross-sections (C5 and C6) are plotted separately rather than merged together. As the load increases, strain discrepancies among the three measuring points on the same cross‑section grow, indicating non‑ideal axial tension and the presence of bending of the middle FRP tubes. For both specimens, the discrepancy is larger at C6 than at C5. At the ultimate load of S1, the maximum discrepancy at C6 (1322.88 με) far exceeds that at C5 (516.09 με); for S3, the values are 2225.22 με at C6 versus 1161.45 με at C5, confirming that bending is more pronounced at the lower end of the middle FRP tube. Additionally, the average strain curve closely follows that of point B, confirming pure bending in the A‑C plane, as observed in the end FMCTCs. At the upper C5, point C records the highest strain and point A the lowest; conversely, at the lower C6, point A is highest and point C lowest, indicating opposite bending states at the two ends.

Comparing S1 and S3, the strain discrepancies within the same cross‑section are consistently larger for S3 at both C5 and C6. At C5, the strains at points A and C relative to the average are 0.96 and 1.05 for S1, versus 0.91 and 1.07 for S3. At C6, the ratios are 1.13 and 0.89 for S1, versus 1.19 and 0.87 for S3. These results show that S3 experienced a more pronounced bending effect than S1, which directly contributed to the differing failure modes of the two specimens.

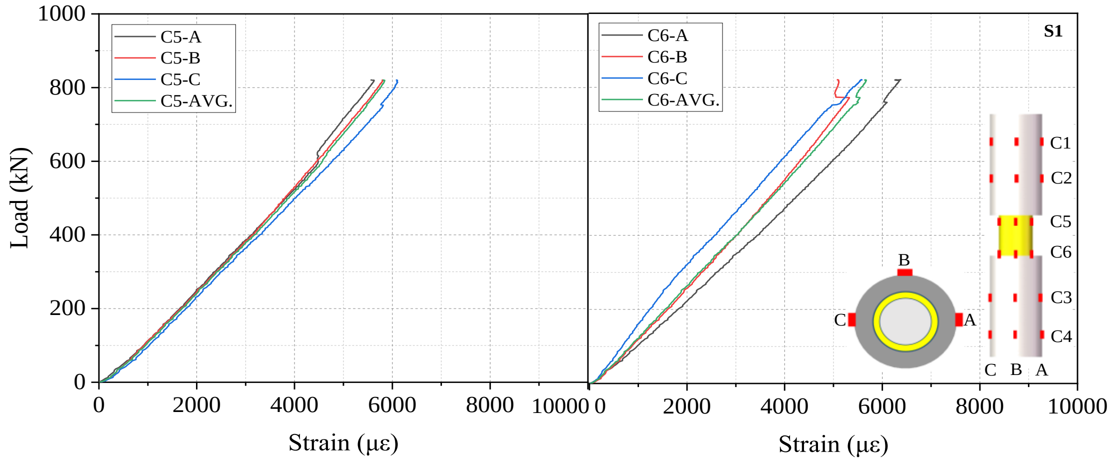

(a) Specimen S1

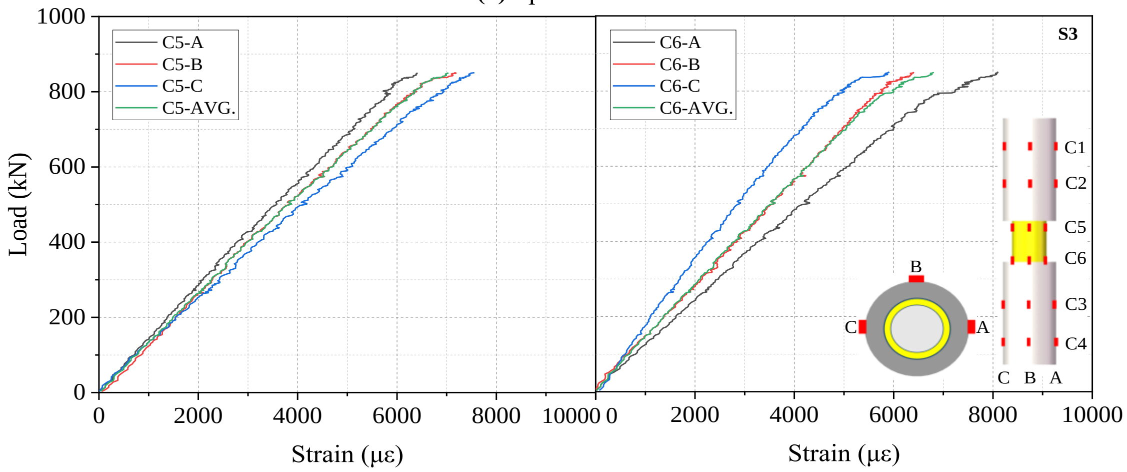

(b) Specimen S3

Fig. 14. Load–strain curves measured by strain gauges positioned on the middle FRP segment.

Table 4 summarizes the maximum measured strain and stress under ultimate load. For both specimens, the peak strain occurred at point A on cross‑section C6: 6390.39 με for S1 and 8107.26 με for S3. Using a longitudinal modulus of 120.0 GPa, the corresponding axial stresses are 766.85 MPa and 972.87 MPa, respectively—both well below the specified FRP tensile strength of 1287.3 MPa. This confirms that S1 experienced no tensile failure of the FRP fibers; instead, shear failure of the FRP threads occurred. For S3, the observed longitudinal cracking and localized sectional fracture may be attributed to an initial localized transverse shear failure at the crimped junction. Furthermore, the load‑displacement curves of the middle FRP tube exhibit nonlinearity near the ultimate load. Despite the brittle nature of pultruded FRP, this nonlinearity is not due to fiber cracking or sectional fracture. Instead, it likely arise from contact nonlinearity at the threaded interface and possibly from progressive shear damage of some FRP threads in the end FMCTCs.

Table 4. Measured maximum strain and stress values on FRP segments under ultimate load

Specimen Number	Section Number	Measured Point Strains (με)				Measured Point Stresses (MPa)			
		A	B	C	Avg.	A	B	C	Avg.
S1	C5	5555.13	5781.57	6071.22	5802.64	666.62	693.79	728.55	696.32
	C6	6390.39	5067.51	5560.44	5672.78	766.85	608.10	667.25	680.73
S3	C5	6395.64	7175.46	7557.09	7034.73	767.48	861.06	906.85	844.17
	C6	8107.26	6402.78	5882.04	6797.36	972.87	768.33	705.84	815.68

5.3.3. Regularity of Strain Evolution

Fig. 15 presents the DIC axial strain contours for specimens S1 and S3 at six loading levels, ranging from 70% to 100% of the ultimate load (F_{ult}). Lagrangian strain is used. Any Lagrangian value can be equivalently expressed in microstrain (με), where 1 με = 10^{-6} (Lagrangian strain). Overall, the maximum strains are concentrated in the middle FRP tube, while lower strains are observed at both end FMCTCs, and all strains remain positive as expected. With increasing load, the peak strain gradually rises. Specimen S1 exhibits a relatively uniform strain distribution in the middle FRP tube, whereas S3 shows a markedly non-uniform strain state. This disparity can be attributed to the fact that while S1 predominantly underwent axial tension, S3 experienced some eccentric loading.

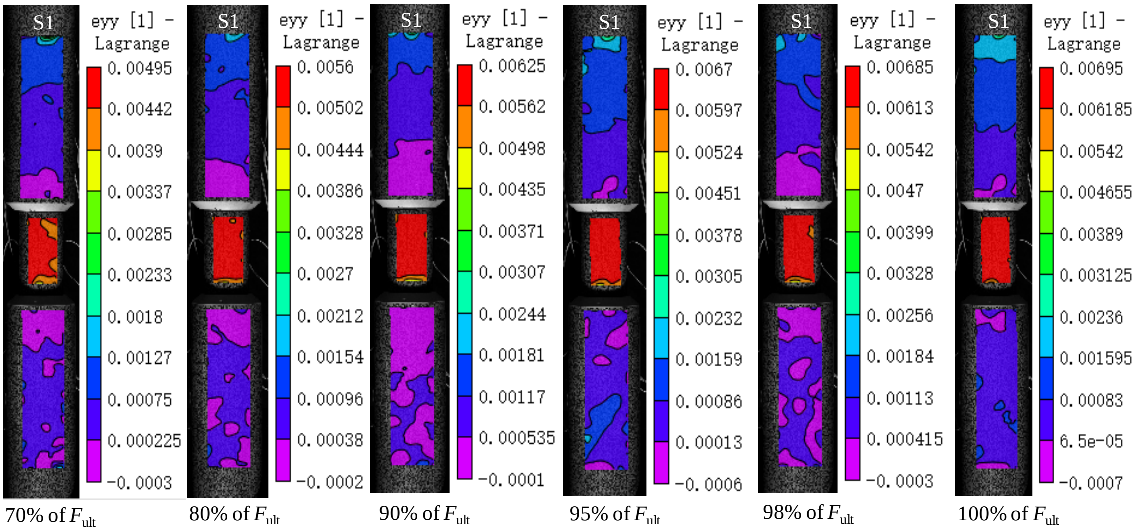

(a) Specimen S1

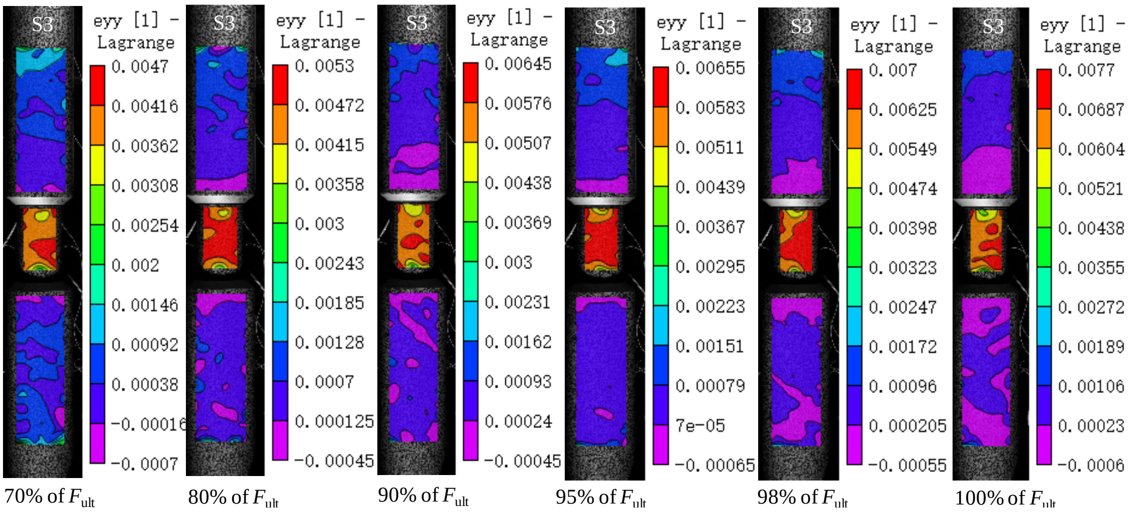

(b) Specimen S3

Fig. 15. Evolution of axial strain contours measured by DIC systems.

For the upper FMCTC of S1, strain magnitudes vary along the tube but with regular boundaries, indicating relatively uniform load transfer. From 70% to 90% of F_{ult},, three distinct regular regions appear, with strain increasing upward—meaning the outer steel sleeve near the UTM fixture transfers more load than near the middle FRP tube, consistent with strain-gauge results. Beyond 90% F_{ult}, local irregularities emerge but the overall pattern remains stable. In contrast, S3's upper FMCTC shows pronounced non-uniformity throughout most loading stages; only at ultimate load do relatively regular strain boundaries appear. For the lower FMCTCs of both specimens, the strain distribution is non-uniform at every load level, with irregular boundaries between regions (e.g., blue and pink regions intersect irregularly). This indicates that the lower FMCTC experiences greater eccentric loading and more complex uneven load transmission than the upper one, likely due to testing-induced eccentricity from the fixed steel connecting piece securing the lower end to the UTM.

Additionally, compressive strains (negative values) are detected in the outer steel sleeves of both specimens, though their absolute values are significantly smaller than tensile strains. They are unevenly distributed and, notably, concentrated at the inner end of both the upper and lower FMCTCs near the middle FRP tube. This concentration results from the outer steel sleeve constraining the interlayered FRP tube. Compressive strains also appear in other regions of the lower FMCTCs. The primary causes are complex spatial effects from eccentric loading and internal end constraints.

Fig. 16 presents the axial strain and deformation contours at peak load for the outer steel sleeves. Compared with the earlier DIC results, these contours show more pronounced unevenness in strain distribution for both the upper FMCTC of S1 and the lower FMCTC of S3, indicating a complex deformation and spatial strain state. In general, strains are smaller near the middle FRP tube and larger near the UTM loading end, consistent with axial deformation. The strain analysis confirms that in S1, the interlayered FRP threads near the loading end failed first, causing a significant load drop (**Fig. 8**); however, with the threads near the middle FRP tube remaining intact, the FMCTC could still sustain some external load. For S3, the observed localized sectional fracture and longitudinal cracks are attributed not only to a more complex strain state due to pronounced eccentric loading and deformation but also to initial manufacturing defects—specifically, local compression and transverse shear damage from forced crimping of the FRP tube within the inner segment of the FMCTC.

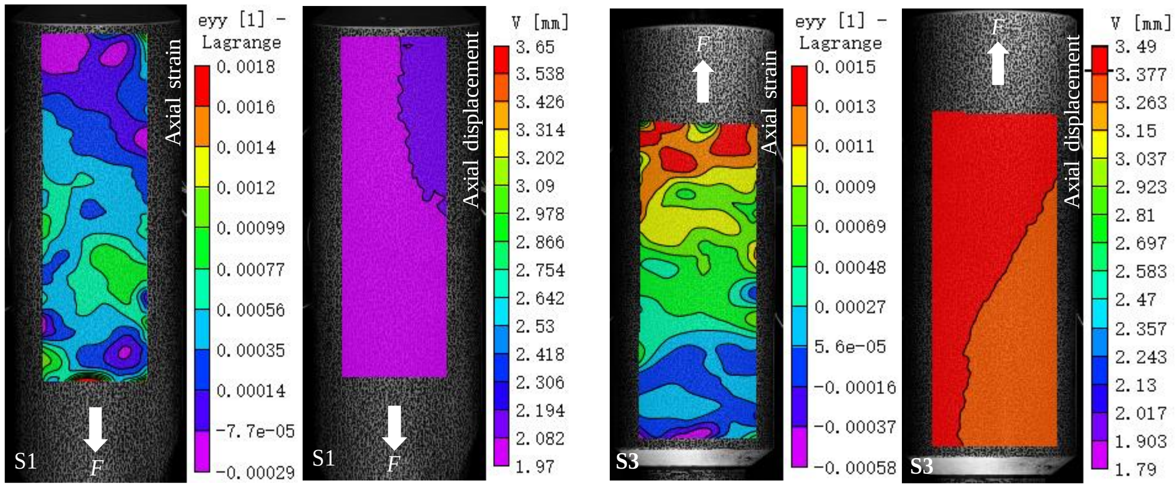

(a) Specimen S1 (b) Specimen S3

Fig. 16. Axial strain and deformation distribution of the outer steel sleeve at the peak load.

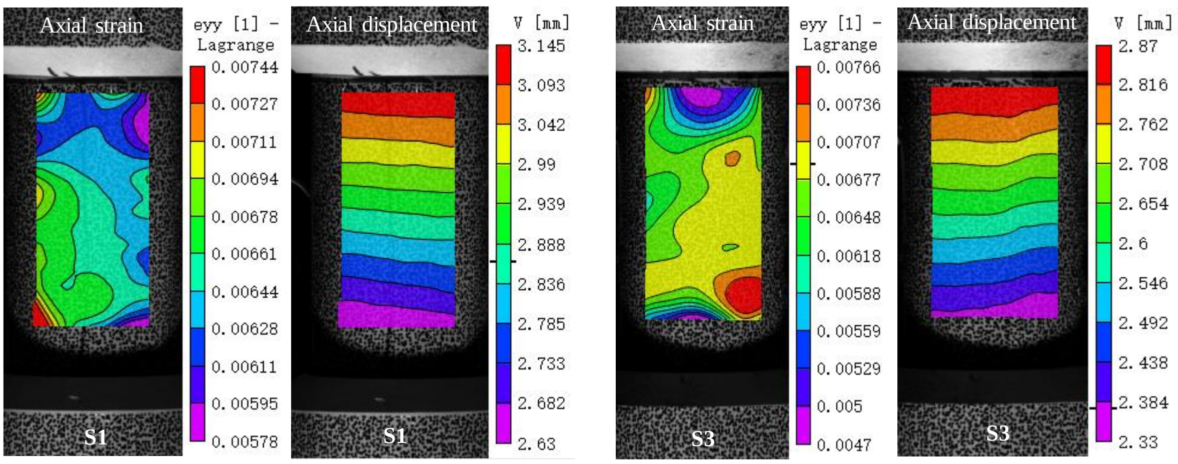

(a) Specimen S1 (b) Specimen S3

Fig. 17. Axial strain and deformation distribution of FRP tube at the peak load.

Fig. 17 presents the axial strain and deformation contours at peak load for the middle FRP tubes. Despite the regular pattern of axial displacement, both specimens S1 and S3 show a complex strain distribution, with the most intricate behavior occurring near the FMCTCs—exhibiting not only varying strain values but also highly irregular boundaries. For instance, the tubular cross-section near the upper connection contains both maximum and minimum strains. This complexity arises from the combined effects of initial damage, eccentric loading, and end constraints.

5.4 Discussions

As mentioned earlier, two distinct failure modes were observed in the specimens. In both cases, axial deformation and strain distribution deviate from ideal axial tension. Aside from possible experimental errors and fabrication defects, the primary direct cause is believed to be the aforementioned eccentric loading. Such eccentric loading and resulting failure likely stem from: misalignment of longitudinal fibers at the crimped junction, initial localized transverse shear failure, inconsistent wall thickness, or inherent uneven distribution of hybrid fibers in the pultruded FRP tube. For example, carbon and glass fibers differ significantly in diameter, causing local variations in packing density (**Fig. 18**). Pultrusion inevitably introduces fiber misalignment and non-uniform fiber distribution, leading to fiber-rich and resin-rich zones, and thus local stiffness and strength heterogeneity.

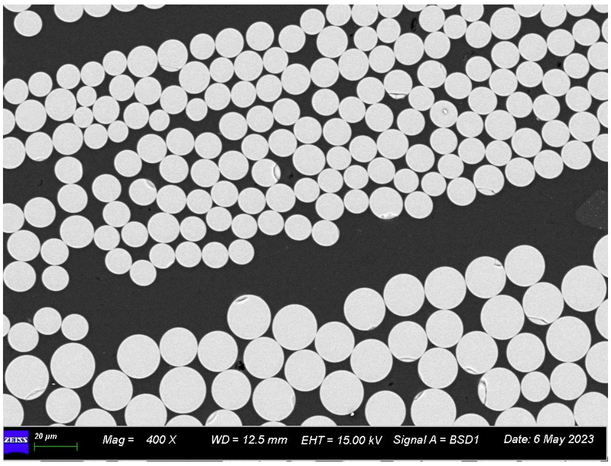

Fig. 18. Microscopic imaging of uneven distribution of hybrid fibers in the pultruded FRP tube.

This local heterogeneity directly governs the mechanical response. Regions with lower fiber content or poor alignment have reduced strength and modulus, causing earlier local failure (resin cracking, debonding, or fiber fracture). This triggers uneven load redistribution and introduces a bending moment even under nominally concentric loading—a 'mechanical eccentricity' inherent to material heterogeneity. Such non-uniformity is an intrinsic characteristic of pultruded FRP, directly governing failure initiation. Progressive failure then propagates from the weak side, manifesting as apparent eccentricity in strain distributions and leading to the observed failure mode transitions (thread shear vs. FRP fracture) and bending effects in the FMCTCs.

These issues are particularly unfavorable because overcoming them poses a significant hurdle in ensuring that the FRP-metal connection can withstand the intended axial loading and function as designed. To prevent misalignment of longitudinal fibers at the crimped junction and initial localized transverse shear failure, reinforcing the tube ends with additional layers of carbon or glass fiber cloth is recommended. To address the inherent uneven distribution of hybrid fibers, post-process inspection is recommended to select specimens with minimal fiber non-uniformity for critical applications. Based on the experimental results, a safety factor of 1.2 is recommended for the connection design in this study to account for the combined eccentricity effects of all contributing irregularities.

A comparison of the FMCTC with the existing CCSJ and PTTC is summarized in **Tab. 5**. The FMCTC achieves a higher and more consistent connection efficiency (65.0%, range: 61.8%–65.0%) than the CCSJ (61.3%, range: 51.2%–61.3% [39]) while maintaining the same low manufacturing complexity and shows less variability. Its failure mode involves shear of FRP threads or FRP fracture, avoiding the interfacial slippage observed in CCSJs and offering more predictable load transfer. Both the FMCTC and CCSJ require no secondary processing of the FRP tube. Although the existing PTTC provides a higher efficiency (≈70%), it comes at the cost of requiring secondary processing of the FRP tube [30–33], which significantly increases fabrication difficulty and quality control efforts. Consequently, the FMCTC strikes a favorable balance among efficiency and manufacturability, making it a promising connection solution for engineering applications.

Table 5. Comparison of FMCTC with existing CCSJ and PTTC systems

Connection type	FMCTC	CCSJ	PTTC
Connection efficiency	65.0%	61.3%	≈70%
Failure modes	Shear of FRP threads vs. FRP fracture	Interfacial slippage	Shear of FRP teeth vs. FRP fracture
Required machining	By crimping the threaded outer sleeve	By crimping the splined outer sleeve	By crimping the toothed outer sleeve
Manufacturing complexity	Requiring no secondary processing of FRP tube	Requiring no secondary processing of FRP tube	Requiring secondary processing of FRP tube

6 Conclusions

The study introduces a new high-tensile FRP-metal connection, specifically engineered for emergency truss bridge applications. Failure tests were conducted to validate the structural feasibility of the configuration and to examine its manufacturing processing, tensile properties, and failure mechanism. The following main conclusions can be drawn:

(1) The proposed FMCTC offers a promising method for connecting FRP tubes, distinguished by a simple manufacturing process and minimal cross-sectional weakening. The circumferential trapezoidal composite threads are produced via forced passive crimping, requiring no secondary processing of the base FRP tube—a key advantage over existing composite connections.

(2) The connection efficiency of the proposed FMCTC is significantly enhanced by the crimped FRP threads, reaching 61.8%–65.0%—outperforming existing CCSJs. Moreover, the circumferential-thread design yields limited bearing capacity variability compared to CCSJs with longitudinal splines.

(3) Two dominant failure modes were identified. The strongest FMCTC failed by localized section fracture and longitudinal cracks in the FRP segment. Axial load transfer is mainly attributed to is mainly attributed to the shear effect of the forced interfacial FRP threads. Despite distinct failure modes, the ultimate bearing capacities showed limited variability across specimens.

(4) Strain analysis revealed complex stress states within the connection, characterized by unintended bending under nominally axial loading. This deviation from idealized uniaxial stress disrupts design-specified axial load transfer and deformation responses of the FMCTCs. Therefore, structural design of the composite connection need optimization.

(5) This study focuses on introducing a new joint configuration and conducting failure tests for feasibility verification. Future work should prioritize developing a numerical model to accurately predict mechanical behavior, despite anticipated complexity. Parametric numerical analyses will be essential for structural optimization and identifying key design parameters.

Acknowledgement

The authors are grateful to the National Key Laboratory for Explosion Shock Disaster Prevention and Mitigation for the research facilities. The authors also gratefully acknowledge the anonymous reviewers for the constructive remarks.

Funding Statement

The authors gratefully acknowledge the financial support provided by National Natural Science Foundation of China (No. 52278230 & 52308295), and Natural Science Foundation of Jiangsu Province (BK20221531).

CRediT authorship contribution statement

Longfa Wang: Investigation, Visualization, Methodology, Writing- original draft. **Dongdong Zhang**: Conceptualization, Data curation, Investigation, Methodology, Funding acquisition, Writing-review & editing. **Ruijie Zhu**: Methodology, Visualization, Funding acquisition. **Yifeng Gao**: Methodology, Funding acquisition, Writing- review & editing. **Chenxi Lv**: Investigation, Data curation, Methodology. **Weite Shi**: Methodology, Resources.

Conflicts of Interest

The authors declare that they have no conflicts of interest to report regarding the present study.

Data Availability Statement

Some or all data, models, or codes that support the findings of this study are available from the corresponding author upon reasonable request.

References

[1] Liu TQ, Liu X, Feng P. A comprehensive review on mechanical properties of pultruded FRP composites subjected to long-term environmental effects. Composites Part B: Engineering 2020; 191: 107958. https://doi.org/10.1016/j.compositesb.2020.107958.

[2] Fang H, Bai Y, Liu WQ, Qi YJ, Wang J. Connections and structural applications of fibre reinforced polymer composites for civil infrastructure in aggressive environments. Composites Part B: Engineering 2019; 164: 129–43. https://doi.org/10.1016/j.compositesb.2018.11.047.

[3] Chen C, Fang H, Han J, Qi YJ. Structural performance evaluation of pultruded GFRP composite space truss: Experimental study and numerical simulation, Case Studies in Construction Materials 2022; 17: e01551. https://doi.org/10.1016/j.cscm.2022.e01551.

[4] Zou XX, Feng Y, Zhong R, Fang TC, Wang JQ. An experimental study of FRP truss side plate joint. Construction and Building Materials 2023; 365:130012. https://doi.org/10.1016/j.conbuildmat.2022.130012.

[5] Zou XX, Wang JQ. Experimental study on joints and flexural behavior of FRP truss-UHPC hybrid bridge. Composite Structures 2018; 203: 414–424. https://doi.org/10.1016/j.compstruct.2018.06.118.

[6] Bai Y, Yang X. Novel joint for assembly of all-composite space truss structures: Conceptual design and preliminary study. Journal of Composites for Construction 2013; 17:130–138. https://doi.org/10.1061/(ASCE)CC.1943-5614. 0000304.

[7] Yang X, Bai Y, Ding FX. Structural performance of a large-scale space frame assembled using pultruded GFRP composites. Composite Structures 2015; 133: 986–996. https://doi.org/10.1016/j.compstruct.2015.07.120.

[8] Hizam RM, Manalo AC, Karunasena W, Bai Y. Behaviour of pultruded GFRP truss system connected using through-bolt with mechanical insert. Composites Part B: Engineering 2019; 168:44–47. https://doi.org/10.1016/ j.compositesb. 2018.12.052.

[9] Zhou XY, Wang NW, Xiong W, Wu WQ, Cai CS. Multi-scale reliability analysis of FRP truss bridges with hybrid random and interval uncertainties. Composite Structures 2022; 297:115928. https://doi.org/10.1016/j.compstruct. 2022.115928.

[10] Teixeira AMAJ, Pfeil MS, Battista RC. Structural evaluation of a GFRP truss girder for a deployable bridge. Composite Structures 2014; 110: 29–38. https://doi.org/10.1016/j.compstruct.2013.11.014.

[11] Higgoda TM, Elchalakani M, Wittek A, Kimiaei M, Yang B. Investigation on the structural failure behaviour of pultruded circular tubular GFRP multiplanar truss bridges with non-metallic connections through finite element modelling. Engineering Failure Analysis 2022; 142: 106739. https://doi.org/10.1016/j.engfailanal.2022.106739.

[12] Li SP, Chen WJ, Hu JH, Zhao B, Zhao HT, Chen LL, Huang XH. Structural design and compression-bending test of ultra-lightweight carbon-fiber-reinforced polymer truss structures. Composite Structures 2023; 313:116909. https://doi.org/10.1016/j.compstruct.2023.116909.

[13] Li SP, Chen WJ, Chen LL, Mi X, Zhang YB. Structural design and axial compression test of novel carbon-fiber-reinforced polymer truss supporting rear connection-ring. Thin-walled structures 2023; 185: 110623. https://doi.org/10.1016/j.tws.2023.110623.

[14] Wight G, Erki MA, Shyu CT, Tanovic R, Heffernan PJ. Development of FRP short-span deployable bridge-experimental results. Journal of Bridge Engineering 2006; 11: 489–498. https://doi.org/10.1061/(ASCE)1084-0702(2006)11:4(489).

[15] Robinson MJ, Kosmatka JB. Development of a short-span fiber-reinforced composite bridge for emergency response and military applications. Journal of Bridge Engineering 2008; 13: 388–397. https://doi.org/10.1061/(ASCE)1084- 0702(2008) 13:4(388).

[16] Pramanik A, Basak AK, Dong Y, Sarker PK, Uddin MS, Littlefair G, et al. Joining of carbon fibre reinforced polymer (CFRP) composites and aluminium alloys – A review. Composites Part A: Applied Science and Manufacturing 2017; 101: 1–29. https://doi.org/10.1016/j.compositesa.2017.06.007.

[17] Wei Y, Jin XH, Luo QT, Li Q, Sun GY. Adhesively bonded joints – A review on design, manufacturing, experiments, modeling and challenges. Composites Part B: Engineering 2024; 2024: 111225. https://doi.org /10.1016/j.compositesb. 2024.111225.

[18] Liu LL, Wang X, Wu ZS, Keller T. Tension-tension fatigue behavior of ductile adhesively-bonded FRP joints. Composite Structures 2021; 268:113925. https://doi.org/10.1016/j.compstruct.2021.113925.

[19] Zhang ZJ, Wu C, Nie X, Bai Y, Zhu L. Bonded sleeve connections for joining tubular GFRP beam to steel member: Numeri-cal investigation with experimental validation. Composite Structures 2016; 157:51–61. https://doi.org/ 10.1016/j.compstruct.2016.08.016.

[20] Qiu CY, Feng P, Yang Y, Zhu L, Bai Y. Joint capacity of bonded sleeve connections for tubular fibre reinforced polymer members. Composite Structures 2017; 163: 267–279. https://doi.org/10.1016/j.compstruct.2016.12.006.

[21] Girão Coelho AM, Mottram JT. A review of the behaviour and analysis of bolted connections and joints in pultruded fibre reinforced polymers. Materials and Design 2015; 74: 86–107. https://doi.org/10.1016/j.matdes.2015.02.011.

[22] Liu CN, Li Y, Chen Y, Li XM, Cao SP, Cheng H, Luo B. Investigation on deformation of composite multi-bolted joints considering influences of hole-location errors and installation sequence. Engineering Failure Analysis 2022; 140: 106592. https://doi.org/10.1016/j.engfailanal.2022.106592.

[23] Luo FJ, Bai Y, Yang X, Lu Y. Bolted sleeve joints for connecting pultruded FRP tubular components. Journal of Composites for Construction 2016; 20:04015024. https://doi.org/10.1061/(ASCE)CC.1943-5614.0000580.

[24] Liu LL, Wang X, Wu ZS, Keller T. Optimization of multi-directional fiber architecture for resistance and ductility of bolted FRP profile joints. Composite Structures 2020; 248: 112535. https://doi.org/10.1016/j.compstruct.2020.112535.

[25] Ding LN, Liu LL, Wang X, Shen HB, Wu ZS. Effects of connecting materials on the static and fatigue behavior of pultruded basalt fiber-reinforced polymer bolted joints. Construction and Building Materials 2021; 273: 121683. https://doi.org/10.1016/j.conbuildmat.2020.121683.

[26] Zhang HY, Zhang L, Liu Z, Qi SJ, Zhu YD, Zhu P. Numerical analysis of hybrid (bonded/bolted) FRP composite joints: A review. Composite Structures 2021; 262: 113606. https://doi.org/10.1016/j.compstruct.2021.113606.

[27] Yokozeki K, Hisazumi K, Vallée T, Evers T, Ummenhofer T, Boretzki J, Albiez M. Hybrid joints consisting of pre-tensioned bolts and a bonded connection, Part II: Large-scale experiments. International Journal of Adhesion and Adhesives 2024; 128: 103523. https://doi.org/10.1016/j.ijadhadh.2023.103523.

[28] Liu LL, Wang X, Wu ZS, Keller T. Resistance and ductility of FRP composite hybrid joints. Composite Structures 2021; 255: 113001. https://doi.org/10.1016/j.compstruct.2020.113001.

[29] Qureshi J, Nadir Y, John SK. Bolted and bonded FRP beam-column joints with semi-rigid end conditions. Composite Structures 2020; 247: 112500. https://doi.org/10.1016/j.compstruct.2020.112500.

[30] Zhang DD, Zhao QL, Li F, et al. Torsional behavior of a hybrid FRP-aluminum space truss bridge: experimental and numerical study. Engineering Structures 2018; 157: 132–143. https://doi.org/10.1016/j.engstruct.2017.12.013.

[31] Zhang DD, Lv YR, Zhao QL, Li F. Development of lightweight emergency bridge using GFRP–metal composite plate-truss girder. Engineering Structures 2019; 196: 109291. https://doi.org/10.1016/j.engstruct.2019.109291.

[32] Zhang DD, Yuan JX, Li F, Lv YR, Zhao QL, Gao YF, Mo CJ, Yang J. Experimental characterization of static behavior of a new GFRP–metal space truss deployable bridge: Comparative case study. Journal of Bridge Engineering 2021; 26(1): 05020011. https://doi.org/10.1061/(ASCE)BE.1943-5592.0001650.

[33] Zhang DD, Yuan JX, Zhao QL, Li F, Gao YF, Zhu RJ, Zhao ZQ. Static performance of a new GFRP–metal string truss bridge subjected to unsymmetrical loads. Steel and Composite Structures 2020; 35: 641–657. https://doi.org/10.12989/ SCS.2020.35.5.641.

[34] Gao YF, Zhang DD, Li F, Zhao QL, Zhao ZQ, Chen Y. Bearing strength and failure behaviour of composite pre-tightened multi-tooth joint. Composite Structures 2021; 272: 114208. https://doi.org/10.1016/j.compstruct.2021.114208.

[35] Li F, Yang WB, Zhao QL, Gao XP, Xu X. Failure analysis of composite pre-tightened teeth joints under bending and tension coupling load. Engineering Failure Analysis 2023; 151: 107408. https://doi.org/10.1016/j.engfailanal.2023.107408.

[36] Gao JG, Zhao QL, Li F, Gao YF, Zhang DD. Fatigue failure investigation of pultruded GFRP pre-tightened single-tooth connector (PTSTC). Engineering Failure Analysis 2019; 106: 104191. https://doi.org/10.1016/

j.engfailanal.2019.104191.
[37] Li F, Zhao QL, Chen HS, Xu LX. Experimental investigation of novel pre-tightened teeth connection technique for composite tube. Steel and Composite Structures 2017; 23:161–72. https://doi.org/10.12989/scs.2017.23.2.161.
[38] Li F, Zhao QL, Liu Z, Zhang DD, Shi L, Duan JH. Load distribution of composite pre-tightened teeth connections embedded with soft layers. Composite Structures 2022; 300:116070. https://doi.org/10.1016/j.compstruct.2022.116070.
[39] Zhang DD, Lv CX. A novel crimped composite spline joint for pultruded FRP tubes: Conceptual design and tensile properties. Thin-walled structures 2024; 202:112112. https://doi.org/ 10.1016/j.tws.2024.112112.